Journal of Geophysical Research: Space Physics

RESEARCH ARTICLE
10.1029/2017JA024871

Key Points:
- 3-D tomography of preseismic ionospheric anomalies
- Positive and negative electron density anomalies in low and high ionosphere
- Anomalies roughly line up along the geomagnetic field

Supporting Information:
- Supporting Information S1

Correspondence to:
L. He,
heliming@mail.neu.edu.cn

Citation:
He, L., & Heki, K. (2018). Three-dimensional tomography of ionospheric anomalies immediately before the 2015 Illapel earthquake, Central Chile. *Journal of Geophysical Research: Space Physics*, *123*. https://doi.org/10.1029/2017JA024871

Received 10 OCT 2017
Accepted 12 APR 2018
Accepted article online 22 APR 2018

Three-Dimensional Tomography of Ionospheric Anomalies Immediately Before the 2015 Illapel Earthquake, Central Chile

Liming He[1,2] **and Kosuke Heki**[2]

[1]Department of Geodesy and Geomatics, School of Resources and Civil Engineering, Northeastern University, Shenyang, China, [2]Department of Earth and Planetary Sciences, Hokkaido University, Sapporo, Japan

Abstract Using ionospheric total electron contents residual data from 146 Global Navigation Satellite System stations in South America, we conducted three-dimensional tomography of ionospheric electron density anomalies immediately before the 2015 Illapel M_w8.3 earthquake, Central Chile. We used five GPS and five GLONASS satellites and applied continuity constraints to regularize the linear least squares inversion. The reconstructed anomalies are composed of positive and negative regions, at altitudes of ~200 km and ~400 km, respectively, distributed roughly along the geomagnetic field. This feature suggests that the observed anomalies occurred by the downward $\boldsymbol{E} \times \boldsymbol{B}$ drift of electrons due to electric fields within ionosphere, possibly caused by surface positive electric charges. We also discuss the existence of the mirror image anomalies near the geomagnetic conjugate point of the epicenter using stations in Colombia.

1. Introduction

Heki (2011) found anomalies of the ionospheric total electron contents (TECs) immediately before large earthquake shortly after the 2011 M_w (moment magnitude) 9.0 Tohoku-oki earthquake from TEC observations using a dense array of Global Navigation Satellite System (GNSS) stations in Japan, GNSS Earth Observation Network. He also found that such TEC anomalies preceded other three large earthquakes, that is, the 1994 M_w8.3 Hokkaido-Toho-Oki earthquake, the 2004 M_w9.2 Sumatra-Andaman earthquake, and the 2010 M_w8.8 Maule earthquake. Heki and Enomoto (2015) further confirmed similar phenomena before all the earthquakes in this century with M_w8.2 or more. Only one exception is the 2005 M_w8.6 Nias earthquake where the ionosphere was highly disturbed by plasma bubble activities. Recently, He and Heki (2017) focused on the earthquakes with smaller moment magnitude. They studied 32 earthquakes with M_w7.0–8.0 in this century and found that 8 earthquakes showed possible preseismic changes starting 20–10 min before earthquakes. In summary, similar cases have been confirmed before 18 earthquakes with moment magnitudes (M_w) 7.3–9.2 up to now.

Statistical analysis of these events showed that (1) the changes in the vertical TEC (VTEC) rates depend on M_w as well as the background absolute VTEC; (2) the anomalies of larger earthquakes tend to have longer precursor times, that is, ~40/20/10 min before M_w9/8/7 earthquakes (He & Heki, 2017; Heki & Enomoto, 2015); and (3) the areal extent of anomalies depend on the fault size of earthquake, that is, the anomalies of larger earthquakes have larger spatial dimensions (He & Heki, 2016). These dependences of anomalies support the reality of the ionospheric TEC anomalies immediately before large earthquakes as precursors.

Three papers opposing our findings have been published (Kamogawa & Kakinami, 2013; Masci et al., 2015; Utada & Shimizu, 2014), but we published rebuttals to them in the same journal with new evidences (Heki & Enomoto, 2013, 2014, 2015). For the detailed summary of the arguments, readers are referred to the introduction of He and Heki (2017).

Two physical models have been proposed to explain the preseismic ionospheric anomalies. Kuo et al. (2014, 2015) considered upward electric current from crust to lower ionosphere made westward electric field within ionosphere and redistributed ionospheric electrons. Kelley et al. (2017), on the other hand, considered that the surface positive charges directly drove the redistribution of ionospheric electrons. In either of the hypotheses, surface positive electric charge makes electric fields within ionosphere, and electron redistributions by downward $\boldsymbol{E} \times \boldsymbol{B}$ drifts. Although the origin of the surface electric charges is not clear, we consider it likely that positive electric charges diffused from stressed rocks play an important role (e.g., Freund, 2011).

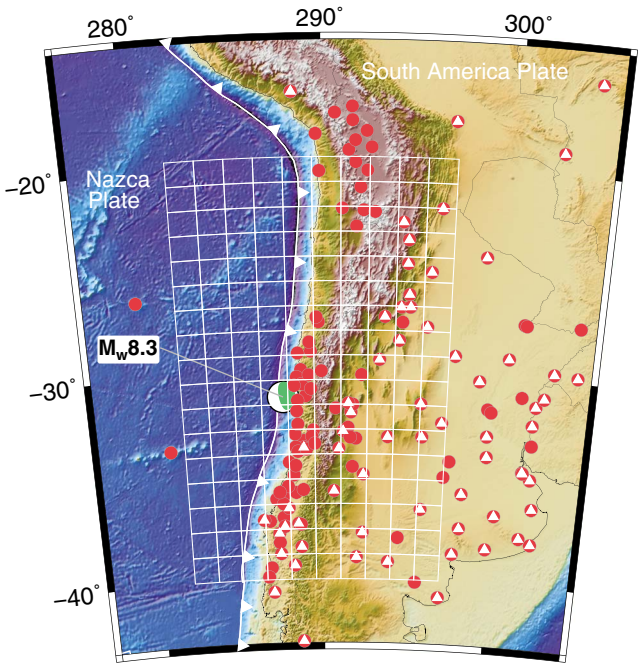

Figure 1. The 146 GPS (red circles) and 65 GPS/GLONASS (white triangles over red circles) stations were used in this study. The white grids show the region to conduct the 3-D ionospheric tomography analysis of the anomalies before the 2015 Illapel earthquake. The green beach ball shows its epicenter and focal mechanism.

Recently, He and Heki (2016) analyzed the spatial distribution of positive and negative ionospheric anomalies immediately before three large earthquakes in Chile, that is, the 2010 Maule (M_w8.8), the 2014 Iquique (M_w8.2), and the 2015 Illapel (M_w8.3) earthquakes. They inferred that the positive and negative electron density anomalies occur in, respectively, lower (altitude ~200 km) and higher (altitude ~400 km) ionosphere, which resembles to the spatial structure of the anomalies made by downward drift of ionospheric electrons (e.g., Kuo et al., 2014).

The computerized ionospheric tomography is an effective way to study the three-dimensional (3-D) structure of ionospheric electron density (Austen et al., 1988). The 3-D tomography requires the availability of observation data with different azimuth and elevation derived from large number of ground stations over an extensive region. Hence, it is possible only in a limited case, such as in South America, where increasing number of permanent GNSS stations are being deployed for crustal deformation studies. Here we perform 3-D tomography of ionospheric anomalies prior to the 2015 Illapel earthquake, Central Chile.

2. The 2015 Illapel Earthquake and the GNSS Data

On 16 September 2015, a M_w8.3 Illapel earthquake ruptured a segment of the Nazca-South America plate boundary in Central Chile (Melgar et al., 2016). It occurred at 19:54 in local time with the epicenter at the geographic latitude of 31.6°S (geomagnetic latitude of 21.7°S). Geomagnetic activity was slightly high at that time, with the *D*st and *Kp* indices of −19 nT and 3, respectively (see Figure S1 of He and Heki (2016)).

Here we use GNSS TEC data derived from raw Receiver Independent Exchange Format (RINEX) data of the 146 GNSS stations in South America (65 of them tracked GLObal NAvigation Satellite System (GLONASS) as well as GPS) from the Centro Sismológico Nacional of Universidad de Chile, the Red Argentina de Monitoreo Satelital Continuo (RAMSC) network of Instituto Geográfico Nacional de Argentina (IGNA), the Rede Brasileira de Monitoramento Contínuo dos Sistemas GNSS (RBMC) network of Instituto Brasileiro de Geografia e Estatística (IBGE), International GNSS Service (www.igs.org), and University NAVSTAR Consortium (www.unavco.org) (Figure 1). We used TEC data from five GPS satellites (12, 14, 15, 24, and 25) and five GLONASS satellites (09, 10, 19, 20, and 21) with relatively high elevation angles.

3. Calculation of GNSS TEC Residual

We first calculate the absolute VTEC for each GNSS satellite-station pair following He and Heki (2016), by removing the satellite and receiver interfrequency biases and multiplying slant TEC (STEC) with the incidence angle into a thin shell at 300 km above the ground. To extract the anomalies relevant to the earthquake, we modeled the VTEC curves with the polynomial of time by excluding a specified time window possibly influenced by the earthquake.

The start of the excluding windows is given, following Heki and Enomoto (2015), by identifying significant positive bends in VTEC time series before earthquakes using the Akaike's information criterion (AIC) (Figure 2a). In calculating −ΔAIC (significance of the bending), we used moving time windows of ±15 minutes and the absolute and relative thresholds of 1 TEC unit (TECU)/hr and 50%, respectively. The thick red curve in the bottom of Figure 2a shows the −ΔAIC for the VTEC time series of GPS satellite 24 at station CMPN. A significant positive break is found ~22 min before the earthquake. The detail of this numerical technique is discussed in section 2.3 of Heki and Enomoto (2015).

The end of the excluding window was set at 25 min after earthquake by visual inspection of the VTEC decrease that may occur after large earthquakes (Figure S1 in the supporting information), for GNSS satellites with high elevation angles (GPS 12 and 24 and GLONASS 9, 10, 19, and 20). Because the intersection of the line-of-sight (LOS) of low-elevation satellites with the ionosphere move away faster from the epicenter, we

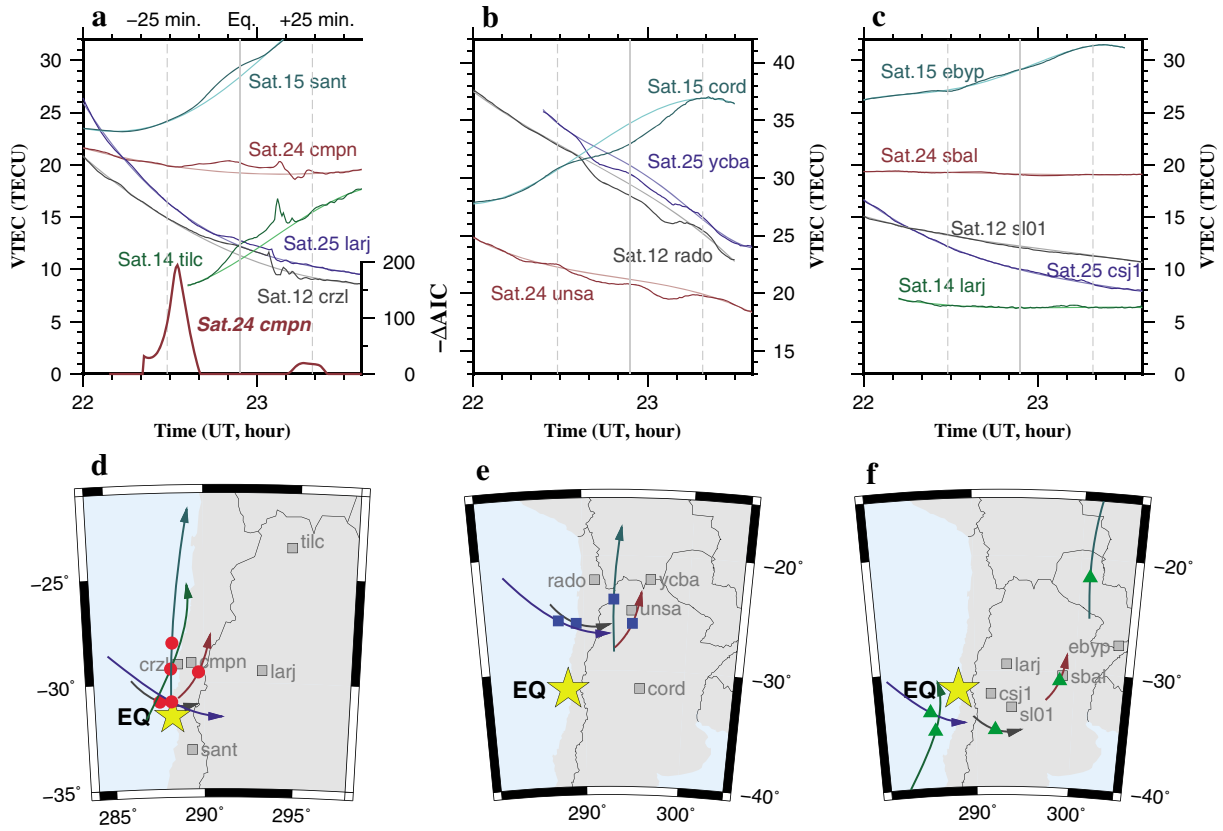

Figure 2. Vertical total electron content (VTEC) time series observed with various Global Navigation Satellite System (GNSS) satellites showing preseismic enhancements (a), decreases (b), and no significant changes (c). The red thick curve in the bottom of (a) shows the −ΔAIC curve to infer the onset time of preseismic VTEC anomalies based on the data of GPS satellite 24 at station CMPN (see Heki & Enomoto, 2015, for details). The vertical gray solid line indicates the occurrence time of the 2015 Illapel earthquake. We plot two vertical dashed lines at ±25 min relative to the main shock for reference. The maps in (d), (e), and (f) show the subionospheric point (SIP) tracks (same colors for same satellites) corresponding to positive, negative and insignificant anomaly curves shown in (a), (b), and (c), respectively. We assume the ionospheric height of 200, 300, and 400 km for positive, insignificant, and negative anomalies to draw the SIP trajectories. We use red circles, blue squares, and green triangles to indicate the earthquake time on the SIP tracks. The gray squares represent the locations of GNSS stations. The yellow star shows the epicenter of the 2015 Illapel earthquake. TECU = total electron content unit.

set the ending time of the excluding time window at 20 min after earthquake for these satellites (GPS 14, 15, and 25 and GLONASS 21).

To avoid the arbitrary selection of polynomial degree of reference curves, we utilized the L-curve method to determine the optimal polynomial degrees for individual GNSS satellites (Figure S2). This procedure, together with the selection of the excluding window, is explained in detail in He and Heki (2017). We show clear TEC enhancements (Figure 2a) and decreases (Figure 2b) starting ~20 min before the earthquake by various GNSS satellites. To illustrate the locality of anomalies, we also show five VTEC time series with SIPs (subionospheric points) far from the epicenter (Figure 2c). They show normal behaviors, that is, the time series do not depart from the reference curves although we set the same excluding time window. We converted all the observations, residuals of VTEC from reference curves, back to STEC and used them as the input to the 3-D tomography.

4. GNSS-Based Ionospheric Tomography

To perform the 3-D tomography of ionospheric electron density anomalies, we divided the local ionosphere into a three-dimensional grid of voxels. Each voxel was bounded in latitude, longitude and altitude, and the electron density anomaly within a voxel was assumed homogeneous. The absolute STEC anomaly observation ($\Delta STEC_i$) along each ray path is approximated as the sum of the product of electron density anomalies per unit length and the penetration length of the voxels, that is,

$$\Delta STEC_i = \sum_{j=1}^{n} a_{ij} x_j + e_i \quad (1)$$

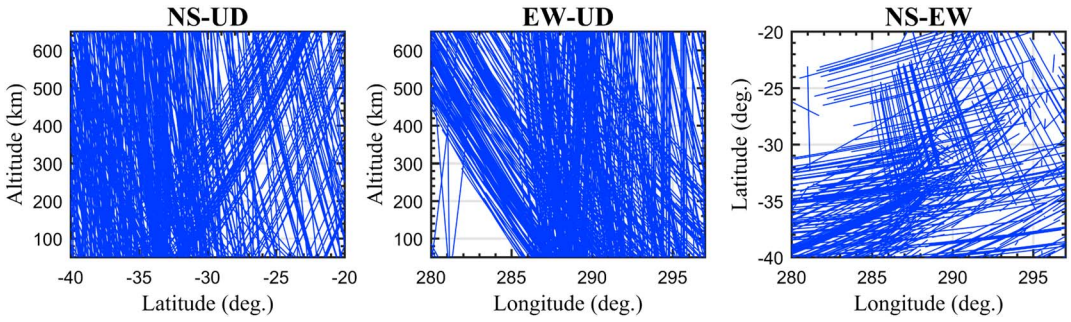

Figure 3. Projection of all the used ray paths connecting Global Navigation Satellite System satellites and stations, onto the three planes corresponding to the region of the 3-D tomography, that is, NS-UD (north-south and up-down), EW-UD (east-west and up-down), and NS-EW (north-south and east-west).

where n is the total number of the voxels, a_{ij} and x_j are the length of ray path and electron density anomaly of the jth voxel, respectively, and e_i is the observational and approximation errors. If the total number of line-of-sights (LOSs) is m, equation (1) can be expressed in matrix form as follows:

$$\mathbf{Y} = \mathbf{AX} + \mathbf{E} \tag{2}$$

where **Y** and **E** are the observation and error vectors with m elements, respectively. The Jacobian matrix with $m \times n$ components is expressed with **A**, and **X** is the electron density anomalies of the n voxels to be estimated.

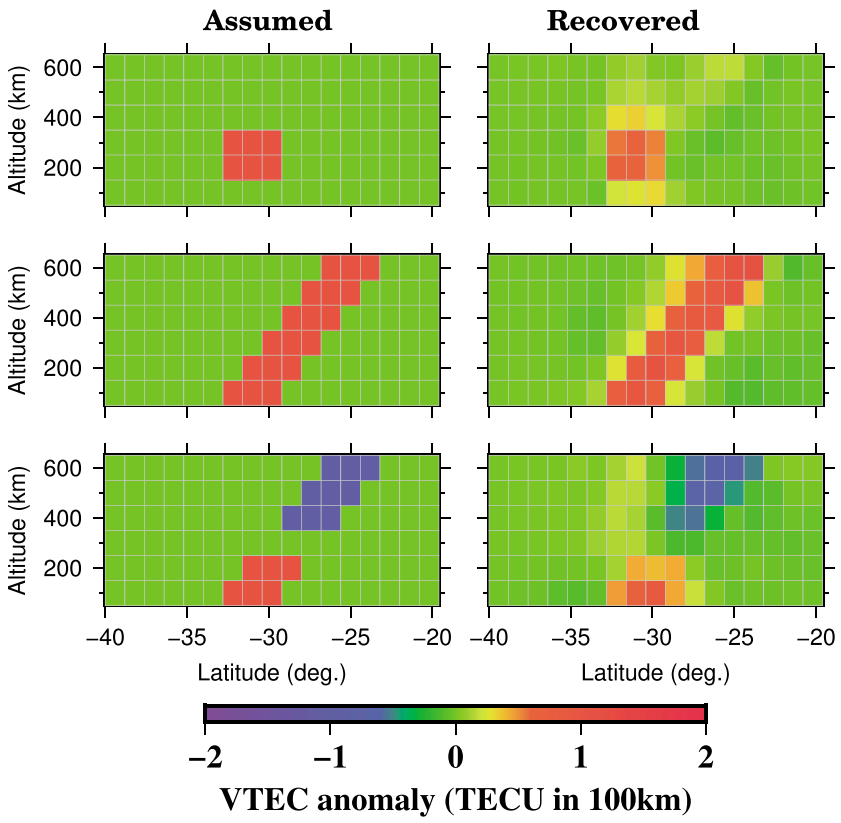

Figure 4. Test to recover three anomaly patterns (left) using synthetic data sets, that is, a block-like positive anomalies (top), a positive anomaly extending along the geomagnetic field (middle), and positive and negative anomalies lying along the geomagnetic field (bottom). We assumed that the east–west (perpendicular to the figure) dimension of the blocks corresponds to three voxels. The patterns are well reproduced by the 3-D tomography (right), shown as the medians of the recovered profiles cutting the anomalies. VTEC = vertical total electron content; TECU = total electron content unit.

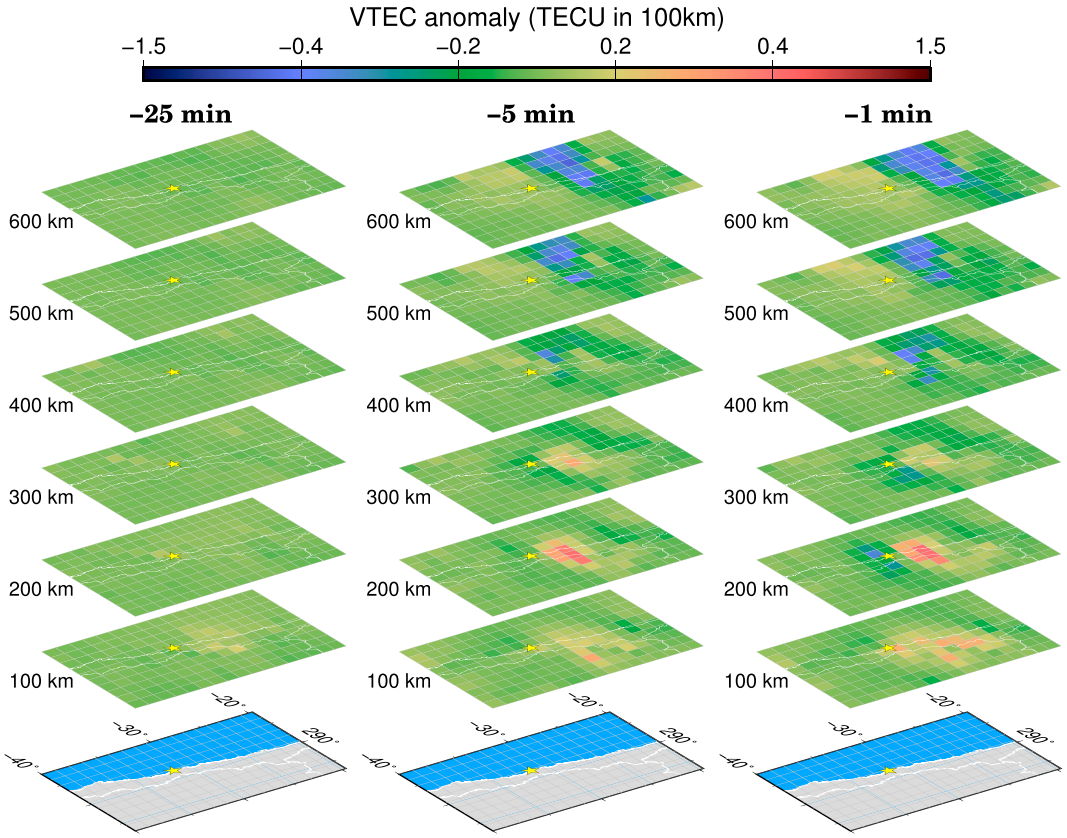

Figure 5. Electron density anomalies at heights from 100 km to 600 km before the 2015 Illapel earthquake derived by the 3-D tomography at three epochs, that is, −25 min (left), −5 min (middle), and −1 min (right). The white curves show coastlines and nation boundaries, and the yellow star indicates the epicenter.

As shown in Figure 1, we set up the voxels as large as 1.5° in longitude, 1.2° in latitude, and 100 km in altitude, over the range from −78°E to −63°E in longitude, from −40°N to −20°N in latitude, and from 50 km to 650 km in altitude. The total number of unknown parameters is ~1,000. Insufficient coverage and density of the ground stations make it difficult to let available LOSs penetrate all the voxels (Figure 3). Although we used both GPS and GLONASS data, the number of available observations is only ~660, and we cannot estimate every component of **X** in (2) by the standard least squares method.

To overcome this, we introduce a continuity constraint, that is, the anomalies of adjacent voxels are constrained to have the same value with a reasonable allowance. We set the allowance as 0.05 (10^{11} el/m^3, a unit equivalent to 1 TECU for a penetration length of 100 km, similar to the voxel size, written as TECU/100 km hereinafter). The STEC observation errors were assumed as 0.05 TECU, a typical error for differential GNSS VTEC measurements (Coster et al., 2013). This is equivalent to adding ~1,000 virtual observations and regularizes the normal matrix in estimating **X** in (2) with the standard linear least squares method. The detail of the 3-D tomography is also available in Muafiry et al. (2018).

5. Resolution Tests With Synthetic Data

To demonstrate the robustness of our tomography results, we conduct a series of tests using synthetic data sets, assuming (1) a block-like positive anomaly, (2) a linear-shaped positive anomaly, and (3) alternating positive and negative anomalies along the geomagnetic field (Figure 4). We use the same GNSS station/satellite geometry as for the 2015 Illapel earthquake occurrence time to synthesize the STEC anomalies. The positive and negative electron density anomalies of the tests are set as $\pm 1 \times 10^{11}$ el/m^3 (TECU/100 km).

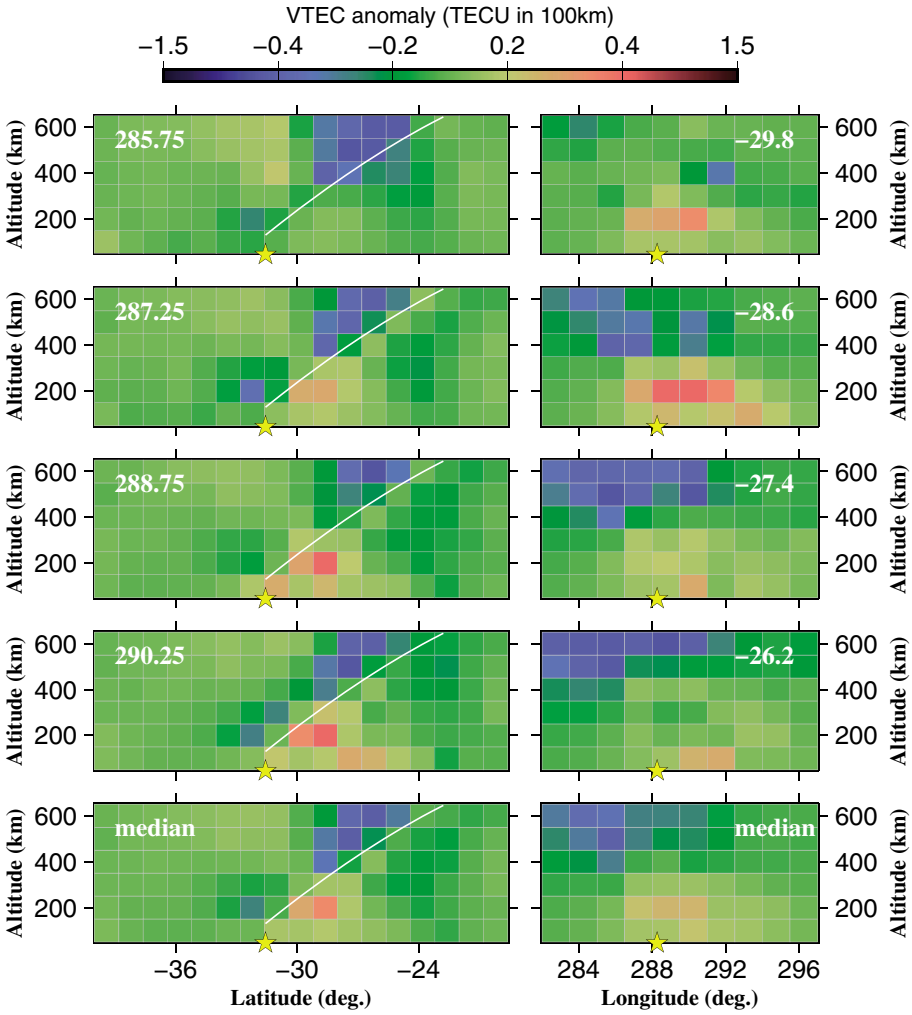

Figure 6. Profiles at longitudes 285.75–290.25, with an interval of 1.5°, of electron density anomalies immediately before the 2015 Illapel earthquake from 3-D tomography (left column). We also show profiles at latitudes from −29.8 to −26.2 with an interval of 1.2° (right column). We show the median of the longitudinal and latitudinal profiles at the bottom. The white curve shows the geomagnetic field, and the yellow star shows the latitude/longitude of the epicenter.

As shown in the right panel of Figure 4, the assumed anomalies are reasonably recovered through our inversion algorithm for the three cases. Difference in the continuity constraint appears in the ambiguity of the anomaly boundaries; that is, a stronger constraint lets the rims blur more, but little in the recovered pattern. We also note that we only have two GNSS stations off the Chilean coast (Figure 1). The insufficient station coverage over the ocean is an inherent drawback for such studies because large earthquakes tend to occur near land-ocean boundaries. In Figure S3, we demonstrate that the anomaly appearing far off the coast is difficult to recover, especially the altitude of the anomaly, due to the shortage of valid ray paths (Figure 3).

We further demonstrate the capability of this inversion method by conducting a classical checkerboard test. The results (Figure S4) suggest that the accuracy is high enough to allow us to detect the spatial structure of local stratified ionospheric anomalies in a robust manner, except in the ionosphere above the northwestern corner of the studied region. We next perform the 3-D tomography analysis using the real GNSS TEC observations to study the spatial structure of ionospheric anomalies preceding the 2015 Illapel earthquake.

6. Tomography Results

Figure 5 presents the tomography results for the six layers of altitudes 100–600 km at three epochs, that is, 25 min, 5 min, and 1 min before the 2015 Illapel earthquake. Although no anomalies are seen at the first

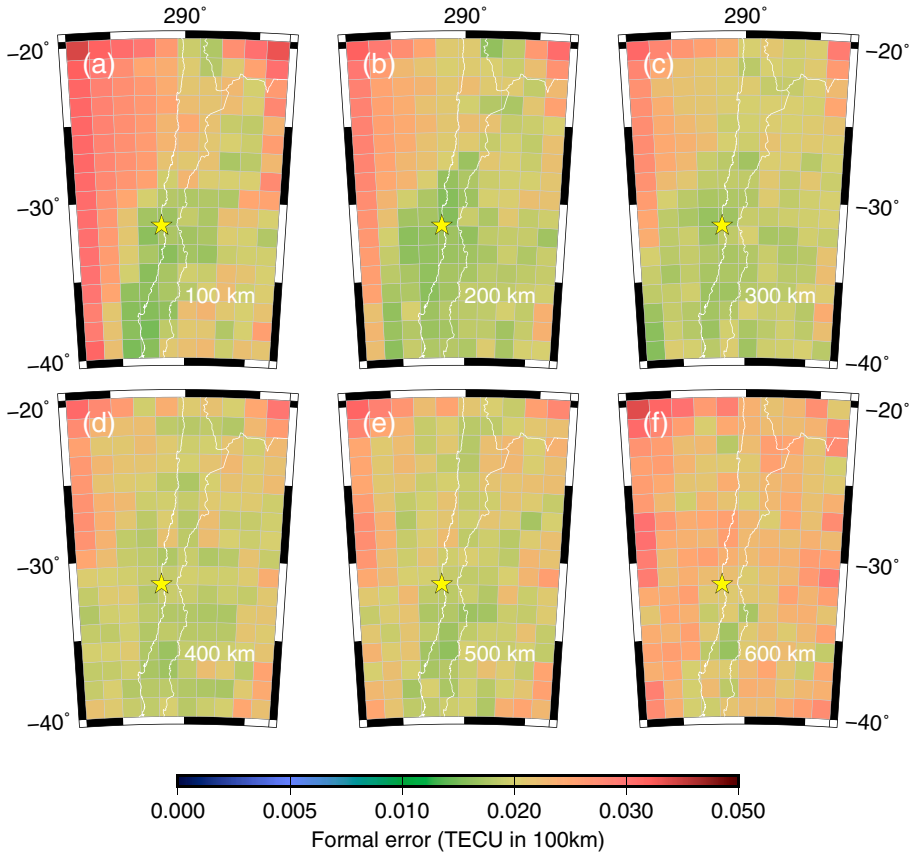

Figure 7. The distribution of errors (square roots of the diagonal components of the inverse of the normal matrix) for layers of altitudes from 100 km (a) to 600 km (f). The errors are relatively small from 200 km to 500 km but increase above the ocean due to the scarcity of Global Navigation Satellite System stations. At 100 km altitude, we see stronger land/ocean accuracy contrast. The yellow star shows the epicenter of the 2015 Illapel earthquake. TECU = total electron content unit.

epoch (Figure 5, left), both positive and negative anomalies have emerged at the second epoch (Figure 5, middle) and grow stronger toward the earthquake time (Figure 5, right). Positive anomalies emerged at lower altitudes about 200 km, while negative anomalies appeared to the north of positive ones at higher altitudes, that is, from 400 km to 600 km.

To visualize the vertical structure of the recovered positive and negative anomalies, we plot selected longitudinal profiles (longitudes: 285.75°, 287.25°, 288.75°, and 290.25°) and latitudinal profiles (latitude: −29.8°, −28.6°, −27.4°, and −26.2°) in Figure 6 (other profiles are given in Figures S5 and S6). Figure 6 also shows medians of the four profiles. The negative anomalies appeared above the positive ones, and the epicenter, the positive anomaly, and the negative anomaly line up roughly along the geomagnetic field, with small downward and upward shifts of the positive and the negative anomalies from the geomagnetic field line (white curves in Figure 6), respectively.

7. Discussions

7.1. Accuracy of the 3-D Tomography

We assess the accuracy of the tomography results from the real data by two different ways, that is, spatial distribution of errors for individual voxels and the standard deviations of the STEC postfit residuals. Formal errors are derived as the square root of the diagonal components of the covariance matrix, and their

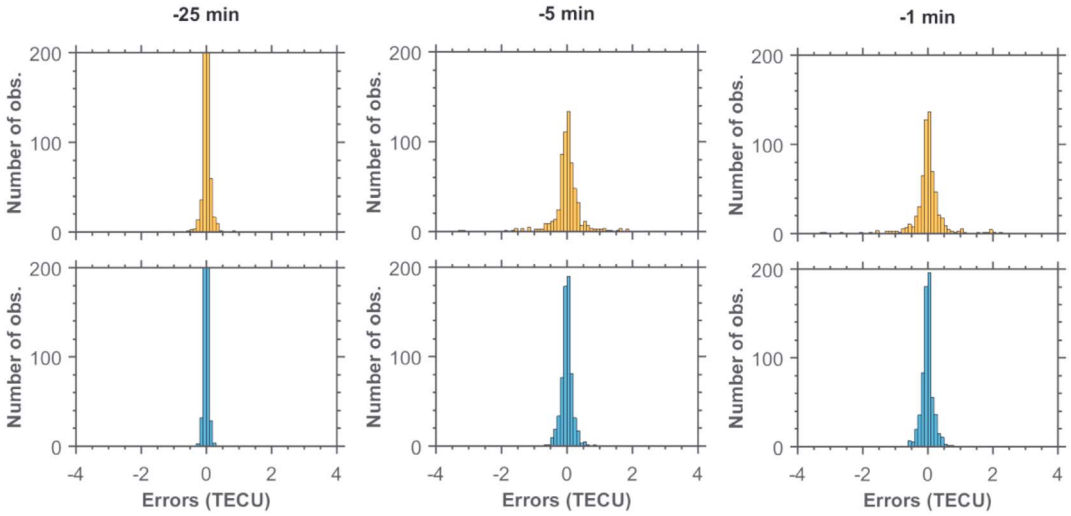

Figure 8. The distribution of observations (upper panel in orange) and postfit residuals (lower panel in blue) of the slant total electron content anomalies at the three epochs, that is, 25 min, 5 min, and 1 min before the 2015 Illapel earthquake. For the epoch with weak anomalies (−25 min), both distributions show small dispersion around 0. For the two epochs with significant anomalies (−5 min and −1 min), the postfit residuals are much smaller, suggesting that our tomography results reproduce the observed slant total electron content anomalies to a certain extent. TECU = total electron content unit.

distribution gives the idea about the nonuniformity of the accuracy. Figure 7 shows relatively high accuracy from l00 to 500 km above land and the lower accuracy of the lowest and the highest layer over the ocean.

To provide an idea of absolute accuracy, we compare the distribution of the input STEC observations with the postfit STEC residuals (Figure 8). For the epoch without anomalies (−25 min), they have similar distribution. For the epochs with anomalies (−5 and −1 min), the residuals have significantly decreased, suggesting that the reconstructed electron density anomalies reproduce the observed STEC data to a certain extent. The standard deviation of postfit residuals is ~0.2 TECU, 4 times as large as the STEC observations errors we assumed earlier. Hence, the absolute errors of the tomography results should be larger than those shown in Figure 7 by a factor of 4 or more.

We further perform a cross validation to directly compare the consistency between the observations and the estimated model parameters. We randomly select 10% of the observations immediately before the earthquake as validation data and perform the 3-D tomography using only the other 90% data. The selected STEC observations (10%) and the STEC values calculated using the estimated parameters are compared in Figure 9. They show good agreements except a few pairs of GPS Satellite 15 and the three Bolivian stations in the northernmost part (bnoe, btnt, and bwsz) of the studied region. The results of the 3-D tomography are less accurate in this region as demonstrated in Figures 7 and S3.

It is meaningful to compare the tomography results with other observation data from different sensors, for example, ionosonde data and GPS radio occultation (RO) measurements. In fact, for the 2011 Tohoku-oki earthquake, Heki and Enomoto (2013) compared the VTEC anomalies with the ionosonde data and the GPS RO data reported in Astafyeva et al. (2011). They showed that the VTEC, geomagnetic declination, and foEs started to change ~40 min before the 2011 Tohoku-oki earthquake. Unfortunately, such comparisons are not possible in the 2015 Illapel earthquake case. There was one ionosonde station (TNJ20) in Tucuman, Argentine, within the studied region, but the data were not available on the day of the earthquake. The nearest GPS RO measurement was >1,000 km away from the studied region within the studied time window.

7.2. Anomalies Above the Geomagnetic Conjugate Point

As suggested in He and Heki (2016), electric fields within ionosphere may be responsible for the redistribution of the ionospheric electrons. This predicts that the same ionospheric TEC anomalies simultaneously emerge in the southern and the northern hemispheres at the geomagnetic conjugate points. Such

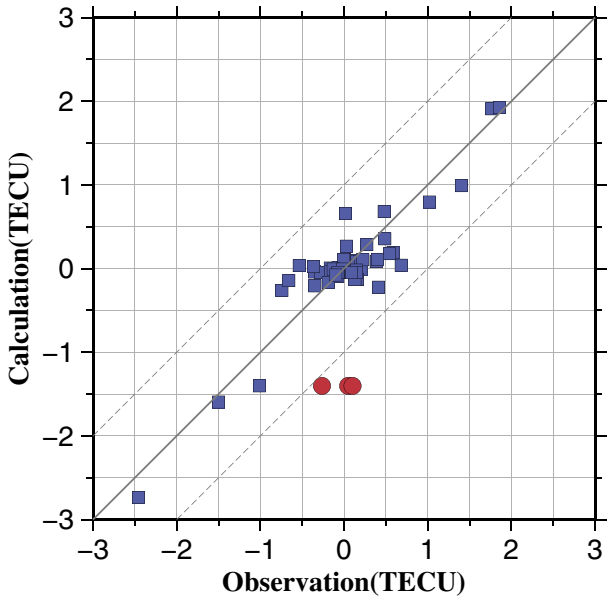

Figure 9. Comparison of the observed slant total electron content anomalies (~10% of the whole data set) immediately before the earthquake (horizontal axis) with those calculated using the parameters estimated without using those data (vertical axis). They mostly fall within ±1 total electron content unit (TECU) from the 45° line. The three data points (red circles) showing large negative deviations (bnoe, btnt, and bwsz stations with the GPS satellite 15) correspond to the northernmost part of the studied area, where the estimated models are inaccurate (Figures 7 and S3).

observations have been difficult so far because of insufficient GNSS station coverage around the conjugate points of the past large earthquakes, for example, the 2011 Tohoku-oki and the 2010 Maule earthquakes. The 2004 Sumatra-Andaman earthquake occurred close to the geomagnetic equator, and the conjugate point of the epicenter lies around the Andaman Islands, the northernmost part of the rupture area (Heki et al., 2006). Hence, that earthquake is not appropriate for the conjugate point study. However, the conjugate point of the 2015 Illapel earthquake epicenter lies in Colombia, South America, where considerable numbers of GNSS stations are available.

We fit the VTEC time series before and after the earthquake using the same method as we did in He and Heki (2017). We found that weak positive ionospheric anomalies seem to have started ~21 min (GARA-Sat.20) before the mainshock there, almost simultaneous with the Chilean anomalies (Figure 10a). We also show four VTEC time series at stations far from the conjugate point to demonstrate that the emergence of possible preseismic anomalies is a local phenomenon in the conjugate region. These TEC curves smoothly connect before and after earthquake although we exclude the same time window (Figure 10b).

Nevertheless, the anomalies in Colombia are too ambiguous to draw firm evidences, that is, many undulations exist due possibly to relatively high geomagnetic activity at that time. After all, we consider the current results inconclusive, that is, difficult to prove or disprove the simultaneous emergence of anomalies in the two hemispheres.

7.3. Physical Mechanisms of the Observed Phenomena

He and Heki (2016) tried to infer the 3-D distribution of ionospheric anomalies before the 2015 Illapel earthquake by projecting the TEC anomalies onto vertical planes running north-south and east-west. Because that method needs low-elevation satellites, only two GPS satellites (14 and 25) were suitable for the purpose. Nevertheless, He and Heki (2016) obtained a rough image that the epicenter, positive anomalies, and negative anomalies align with the geomagnetic field. The 3-D tomography in the present study enabled us to clarify the 3-D structure of the anomalies in a more robust manner.

Two physical models have been proposed to explain the ionospheric anomalies immediately before large earthquake. The numerical simulation studies by Kuo et al. (2014) demonstrated that the upward electric current from lithosphere into ionosphere makes a westward electric field and downward $\boldsymbol{E} \times \boldsymbol{B}$ drifts of ionospheric electrons. However, this model needs an unrealistically strong vertical electric field near the surface. The recent study by Kelley et al. (2017), on the other hand, suggested that the electric field made directly by the surface electric charges could redistribute ionospheric electrons through the $\boldsymbol{E} \times \boldsymbol{B}$ drifts.

In spite of the difference in the mechanisms to make the electric field, they both assume that the electric field plays the major role to redistribute ionospheric electrons immediately before earthquake. Consequently, they both predict similar spatial distribution of the positive/negative anomalies and the existence of the mirror image above the geomagnetic conjugate point. Here we showed that the 3-D distribution of positive and negative anomalies above the epicenter is consistent with these mechanisms, although the mirror image anomaly above the magnetic conugate point cannot be demonstrated with a convincing evidence.

What we need next would be to identify the mechanism to generate positive electric charges above the ground immediately before large earthquakes. Laboratory experiments with rock samples show that positive hole charge carriers are activated associated with the growth of microscopic cracks and dislocations caused by strong stress (e.g., Freund, 2011). Its occurrence during an earthquake nucleation process may lead to the accumulation of surface positive electric charges over the ground immediately before earthquake. Detections of their signatures for real earthquakes by a certain kind of geophysical sensors would make a breakthrough in understanding the physical mechanism behind the series of phenomena.

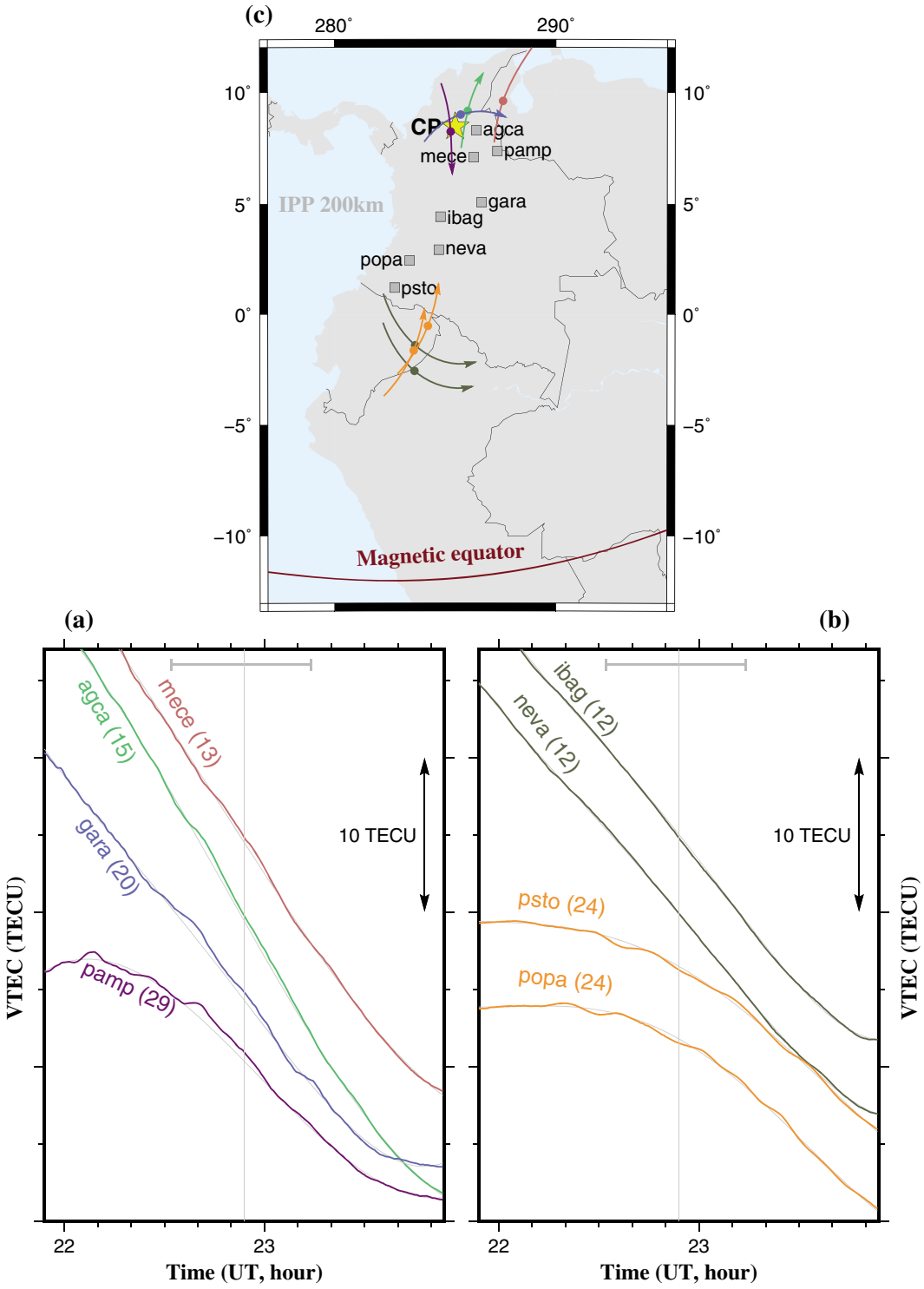

Figure 10. (a) Vertical total electron content (VTEC) time series observed at four Global Navigation Satellite System (GNSS) stations in northern Colombia (gray squares) using GPS satellites 13, 15, 20, and 29, suggesting the existence of positive preseismic anomalies near the geomagnetic conjugate point of the epicenter of the 2015 Illapel earthquake. The vertical gray line represents the earthquake occurrence time. The horizontal gray bar at the top shows the time window (−22 min to +20 min) excluded in defining the reference curves (thin gray curves). (b) VTEC time series using GPS satellites 12 and 24 showing no anomalies at four GNSS stations in southern Colombia (gray squares) far from the conjugate point. (c) The map shows the trajectories of the subionospheric point assuming the ionospheric penetration point height at 200 km. The circles on the trajectories show the subionospheric point positions at the earthquake time. The red curve shows the magnetic equator. We think that the signals in (a) are too weak to draw a firm conclusion regarding the existence of anomalies near the geomagnetic conjugate point.

Acknowledgments
We thank all the reviewers for constructive comments. Liming He was supported by the China Scholarship Council (CSC) and by the National Natural Science Foundation of China (grants 41104104 and 41771416). The authors are grateful to the Centro Sismológico Nacional (CSN) of Universidad de Chile and the Instituto Geográfico Agustín Codazzi (IGAC) of Colombia for providing private GNSS data in Chile and Colombia, respectively. We downloaded the Argentine GNSS data from IGNA (http://ign.gob.ar) and the Brazilian GNSS data from IBGE (https://www.ibge.gov.br). We downloaded additional data from IGS (http://www.igs.org) and UNAVCO (http://www.unavco.org).

References

Astafyeva, E., Lognonné, P., & Rolland, L. (2011). First ionospheric images of the seismic fault slip on the example of the Tohoku-oki earthquake. *Geophysical Research Letters*, *38*, L22104. https://doi.org/10.1029/2011GL049623

Austen, J. R., Franke, S. J., & Liu, C. (1988). Ionospheric imaging using computerized tomography. *Radio Science*, *23*(3), 299–307. https://doi.org/10.1029/RS023i003p00299

Coster, A., Williams, J., Weatherwax, A., Rideout, W., & Herne, D. (2013). Accuracy of GPS total electron content: GPS receiver bias temperature dependence. *Radio Science*, *48*, 190–196. https://doi.org/10.1002/rds.20011

Freund, F. T. (2011). Pre-earthquake signals: Underlying physical processes. *Journal of Asian Earth Sciences*, *41*(4-5), 383–400. https://doi.org/10.1016/j.jseaes.2010.03.009

He, L., & Heki, K. (2016). Three-dimensional distribution of ionospheric anomalies prior to three large earthquakes in Chile. *Geophysical Research Letters*, *43*, 7287–7293. https://doi.org/10.1002/2016GL069863

He, L., & Heki, K. (2017). Ionospheric anomalies immediately before M_w 7.0–8.0 earthquakes. *Journal of Geophysical Research: Space Physics*, *122*, 8659–8678. https://doi.org/10.1002/2017JA024012

Heki, K. (2011). Ionospheric electron enhancement preceding the 2011 Tohoku-Oki earthquake. *Geophysical Research Letters*, *38*, L17312. https://doi.org/10.1029/2011GL047908

Heki, K., & Enomoto, Y. (2013). Preseismic ionospheric electron enhancements revisited. *Journal of Geophysical Research: Space Physics*, *118*, 6618–6626. https://doi.org/10.1002/jgra.50578

Heki, K., & Enomoto, Y. (2014). Reply to comment by K. Heki and Y. Enomoto on "Preseismic ionospheric electron enhancements revisited". *Journal of Geophysical Research: Space Physics*, *119*, 6016–6018. https://doi.org/10.1002/2014JA020223

Heki, K., & Enomoto, Y. (2015). M_w dependence of the preseismic ionospheric electron enhancements. *Journal of Geophysical Research: Space Physics*, *120*, 7006–7020. https://doi.org/10.1002/2015JA021353

Heki, K., Otsuka, Y., Choosakul, N., Hemmakorn, N., Komolmis, T., & Maruyama, T. (2006). Detection of ruptures of Andaman fault segments in the 2004 great Sumatra earthquake with coseismic ionospheric disturbances. *Journal of Geophysical Research*, *111*, B09313. https://doi.org/10.1029/2005JB004202

Kamogawa, M., & Kakinami, Y. (2013). Is an ionospheric electron enhancement preceding the 2011 Tohoku-Oki earthquake a precursor? *Journal of Geophysical Research: Space Physics*, *118*, 1751–1754. https://doi.org/10.1002/jgra.50118

Kelley, M. C., Swartz, W. E., & Heki, K. (2017). Apparent ionospheric total electron content variations prior to major earthquakes due to electric fields created by tectonic stresses. *Journal of Geophysical Research: Space Physics*, *122*, 6689–6695. https://doi.org/10.1002/2016JA023601

Kuo, C. L., Lee, L. C., & Heki, K. (2015). Preseismic TEC changes for Tohoku-oki earthquake: Comparisons between simulations and observations. *Terrestrial, Atmospheric and Oceanic Sciences*, *26*(1), 63–72. https://doi.org/10.3319/TAO.2014.08.19.06(GRT)

Kuo, C. L., Lee, L. C., & Huba, J. D. (2014). An improved coupling model for the lithosphere-atmosphere-ionosphere system. *Journal of Geophysical Research: Space Physics*, *119*, 3189–3205. https://doi.org/10.1002/2013JA019392

Masci, F., Thomas, J., Villani, F., Secan, J., & Rivera, N. (2015). On the onset of ionospheric precursors 40 min before strong earthquakes. *Journal of Geophysical Research: Space Physics*, *120*, 1383–1393. https://doi.org/10.1002/2014JA020822

Melgar, D., Fan, W., Riquelme, S., Geng, J., Liang, C., Fuentes, M., et al. (2016). Slip segmentation and slow rupture to the trench during the 2015, M_w8. 3 Illapel, Chile earthquake. *Geophysical Research Letters*, *43*, 961–966. https://doi.org/10.1002/2015GL067369

Muafiry, I. N., Heki, K., & Maeda, J. (2018). 3D tomography of midlatitude sporadic-E in Japan from GNSS-TEC data. *Earth, Planets and Space*, *70*(1). https://doi.org/10.1186/s40623-018-0815-7

Utada, H., & Shimizu, H. (2014). Comment on "Preseismic ionospheric electron enhancements revisited" by K. Heki and Y. Enomoto. *Journal of Geophysical Research: Space Physics*, *119*, 6011–6015. https://doi.org/10.1002/2014JA020044